



Article

# Luminescent Lanthanide Metal Organic Frameworks as Chemosensing Platforms towards Agrochemicals and Cations

Germán E. Gomez <sup>1,2,\*</sup>, María dos Santos Afonso <sup>3,4</sup>, Héctor A. Baldoni <sup>5</sup>, Federico Roncaroli <sup>6</sup> and Galo J. A. A. Soler-Illia <sup>4,7,\*</sup>

- <sup>1</sup> Gerencia Química, Centro Atómico Constituyentes, Comisión Nacional de Energía Atómica, Avenida General Paz 1499, San Martín, Buenos Aires 1650, Argentina
  - <sup>2</sup> Instituto de Investigaciones en Tecnología Química (INTEQUI), Área de Química General e Inorgánica, Facultad de Química, Bioquímica y Farmacia, Chacabuco y Pedernera, Universidad Nacional de San Luis, San Luis 5700, Argentina
  - <sup>3</sup> Departamento de Química Inorgánica, Analítica y Química Física, Facultad de Ciencias Exactas y Naturales, Universidad de Buenos Aires, Ciudad Universitaria Pabellón II 3er Piso, Intendente Guiraldes, Ciudad Autónoma de Buenos Aires C1428EGA, Argentina; dosantos@qi.fcen.uba.ar
  - <sup>4</sup> Instituto de Química Física de los Materiales, Medio Ambiente y Energía (INQUIMAE)-CONICET, Ciudad Universitaria Pabellón II 3er Piso, Intendente Guiraldes, Ciudad Autónoma de Buenos Aires C1428EGA, Argentina
  - <sup>5</sup> Instituto de Matemática Aplicada de San Luis (IMASL), Área de Química General e Inorgánica, Facultad de Química, Bioquímica y Farmacia, Chacabuco y Pedernera, Universidad Nacional de San Luis, San Luis 5700, Argentina; hbaldoni@unsl.edu.ar
  - <sup>6</sup> Departamento de Física de Materia Condensada, Centro Atómico Constituyentes, Comisión Nacional de Energía Atómica (CNEA), Avenida General Paz 1499, San Martín, Buenos Aires 1650, Argentina; f\_roncaroli@hotmail.com
  - <sup>7</sup> Instituto de Nanosistemas, Universidad Nacional de San Martín-CONICET, Av. 25 de Mayo 1021, San Martín, Buenos Aires 1650, Argentina
- \* Correspondence: gegomez@unsl.edu.ar (G.E.G.); gsoler-illia@unsam.edu.ar (G.J.A.A.S.-I.)

Received: 11 February 2019; Accepted: 7 March 2019; Published: 12 March 2019



**Abstract:** Since the first studies of luminescent sensors based on metal organic frameworks (MOFs) about ten years ago, there has been an increased interest in the development of specific sensors towards cations, anions, explosives, small molecules, solvents, etc. However, the detection of toxic compounds related to agro-industry and nuclear activity is noticeably scarce or even non-existent. In this work, we report the synthesis and characterization of luminescent lanthanide-based MOFs (Ln-MOFs) with diverse crystalline architectures obtained by solvothermal methods. The luminescent properties of the lanthanides, and the hypersensitive transitions of  $\text{Eu}^{3+}$  ( $^5\text{D}_0 \rightarrow ^7\text{F}_2$ ) and  $\text{Tb}^{3+}$  ( $^5\text{D}_4 \rightarrow ^7\text{F}_5$ ) intrinsically found in the obtained MOFs in particular, were evaluated and employed as chemical sensors for agrochemical and cationic species. The limit of detection (LOD) of Tb-PSA MOFs (PSA = 2-phenylsuccinate) was 2.9 ppm for  $[\text{UO}_2^{2+}]$  and 5.6 ppm for  $[\text{Cu}^{2+}]$ . The variations of the 4f–4f spectral lines and the quenching/enhancement effects of the Ln-MOFs in the presence of the analytes were fully analyzed and discussed in terms of a combinatorial “host–guest” vibrational and “in-silico” interaction studies.

**Keywords:** metal organic frameworks (MOFs); sensing; luminescence; lanthanides

## 1. Introduction

In early studies, metal organic frameworks (MOFs) and coordination polymer (CP) compounds have been the center of an intensely developed field due to their emerging applications in ion exchange and gas separation [1] and heterogeneous catalysis [2–5]. In addition, the possibility of using a diversity of structural building blocks allows chemists to design these frameworks in order to exploit specific and/or tunable properties stemming from the ions, the molecular linkers, and their connectivity and synergy. In this sense, lanthanide ions are of special interest in photonics and magnetism because of their unique optical features derived from 4f–4f transitions which include narrow signals and a wide range of lifetime values, frequently accompanied with high quantum yields (QYs) [6–8]. These features are important in materials science for the specific design of phosphors [9], the generation and amplification of light in lasers [10], optical amplifiers [11], solid-state lighting (SSL), full color displays, and backlights [12–14]. Moreover, the hypersensitive transitions [15] found in some lanthanides enable Ln-MOFs and/or Ln-CPs to be suitable candidates for the elaboration of thermo- [16,17] or chemical sensors for toxic substances [18]. In particular, the  $^5D_0 \rightarrow ^7F_2$  in  $\text{Eu}^{3+}$  and  $^5D_4 \rightarrow ^7F_5$  in  $\text{Tb}^{3+}$  are the most reliable and robust signals for those proposals (see Supplementary Material Section 1) [19,20].

On the other hand, microporous MOFs are an attractive kind of materials that exhibit fascinating environment-responsive properties, such as “breathing” and “swelling”, which are involved in selective sorption and controlled release of molecules from MOFs used in sensing and drug delivery, respectively [21]. Given the richness of terminal functional groups of the linkers and solvent molecules within MOFs to induce H-bonding interactions with guest species, open frameworks are expected to be promising materials for chemical sensing. There are already remarkable examples of 3D, open structures such as Ln-BTC (BTC = 1,3,5-benzenetricarboxylate) acting as cationic [22] or small molecule [23] sensors. Moreover, the set of Ln-BPDC phases ( $\text{Ln}^{3+} = \text{Tb}, \text{Ho}, \text{Er}$  and  $\text{Y}$ ; BPDC = 4,4'-biphenyldicarboxylate) presents one-dimensional micropores which are suitable for sensing assays [24].

Contrary to open frameworks such as zeolites and MOF materials, some structures, such as 3D or 2D CPs, cannot exhibit the “confinement effect” [25]. Nevertheless, their optical properties could be useful for sensing due to the hypersensitive nature of the luminescence of their components. Three examples of dense lanthanide-based frameworks with sensing applications obtained in our group are the 3D europium carboxylate which has been used to sense small solvents; [26] meanwhile, the 2D mixed compound,  $\text{EuTb-PSA}$  (PSA = 2-phenylsuccinate), was employed as a thermometric sensor in the 13.5–313.5 K range [27]. In addition, a 1D framework was recently obtained by us and studied as a chemical sensor towards Volatile Organic Compounds (VOCs) with excellent results [28]. Moreover, a new 2D mixed phase doped with  $\text{Eu}$  and  $\text{Tb}$  was synthesized and tested as a chemosensor for small molecules showing selectivity towards carbonyl compounds [29].

As it is necessary to design new methodologies to detect toxic and dangerous compounds in an accurate way, the use of luminescent MOFs (LMOFs) seems to be a reliable pathway to non-conventional sensor platforms [18]. In the recent literature, there are many examples of LMOFs as sensors of explosives, cations, anions, solvents, and VOCs, among others [30], but strikingly, there have been no reports for agrochemical sensing. This is indeed a strategic field due to the need for more efficient methods of mass food production. In addition, periodic or prolonged contact with agrochemicals has been documented to lead to negative effects on human health, such as neuronal illnesses (fungicides, insecticides, and fumigants), cancer, immunologic abnormalities, and reproductive damage (pesticides) [31,32].

Given the nearly limitless choices of building block combinations, MOFs thrive on structural diversity and tunable chemical and physical exceptional properties. The permanent porosity in a large set of MOFs further enables the adsorption of guest molecules, enhancing host–guest interactions. The pore size, shape, chemical composition, surface, and molecular environment can be finely tuned, potentially facilitating the selective seizing of certain guest molecules. This merit of MOFs is the foundation of many well-explored applications, especially in gas storage and separation fields.

In addition, the perturbation from adsorbed guest molecules can alter the photoluminescence in LMOFs, making great candidates for chemosensing.

For LMOFs, in principle, any change in their spectroscopic characteristics can potentially be used as a sensing signal. While the most commonly used feature is the fluorescence intensity, depending on the electronic nature of the molecule being detected (analyte), either quenching or enhancement of the luminescence can be exploited. These changes can be attributed to either electron transfer or energy transfer (ET) between the analyte species and the LMOF, or a combination of both [33–36]. Nitroaromatic compounds, such as explosive-like molecules, are known as strong quenchers due to their high electron affinity [37]. In addition, paramagnetic metal ions (i.e.,  $\text{Cu}^{2+}$ ,  $\text{Mn}^{2+}$ ,  $\text{Ni}^{2+}$ ,  $\text{Co}^{2+}$ ) are also capable of quenching fluorescence since they can facilitate ligand to metal charge transfer (LMCT) and relax the excitation energy through non-radiative pathways [38,39]. In contrast, electron-rich molecules such as benzene and its derivatives with electron-donating substituents, can efficiently enhance fluorescence due to their ability to donate an electron from an excited state to the LUMO (conduction band) of the LMOF [40,41].

In this work we present an in-depth study of the sensor activity of two 3D LMOFs, **Eu-BTC** and **Eu-BPDC**, and two layered CPs, **Eu-PSA** and **Tb-PSA**, obtained by solvothermal method. All compounds were fully characterized by X-ray powder diffraction (PXRD), vibrational spectroscopy (FTIR), thermal analysis (TGA-DSC), and scanning electron microscopy (SEM). Regarding the optical features of these materials, their chemical sensor activities were evaluated on the basis of the influence of diverse agrochemicals and cationic species on the lanthanides hypersensitive  $^5\text{D}_0 \rightarrow ^7\text{F}_2$  and  $^5\text{D}_4 \rightarrow ^7\text{F}_5$  signals. All these studies mark the route for the rational design of luminescent Ln-MOFs and set the basis for building specific optical devices based on pre-designed components with synergetic, adsorptive-luminescent functionality.

## 2. Materials and Methods

Caution: Whereas the uranium nitrate ( $\text{UO}_2(\text{NO}_3)_2 \times 6\text{H}_2\text{O}$ ) used in this study consists of depleted U, standard precautions for handling radioactive and toxic substances should be followed. The same guidelines were carried out when agro-toxics were used.

### 2.1. Synthesis of Sensor Materials

The sensor materials were obtained as crystalline solids under solvothermal conditions using 43 or 120 mL Teflon-lined Parr reactors. Crystalline samples of  $[\text{Eu}_2(\text{C}_{10}\text{H}_8\text{O}_4)_3(\text{H}_2\text{O})]$  (**Eu-PSA** or **Tb-PSA**,  $[\text{Eu}_2(\text{C}_{14}\text{H}_8\text{O}_4)_3(\text{H}_2\text{O})_2]$ , DMF (**Eu-BPDC**) and  $[\text{Eu}_2(\text{C}_9\text{H}_3\text{O}_4)_3(\text{H}_2\text{O})] \times \text{DMF}$  (**Eu-BTC**) were prepared according to procedures similar to those previously reported [24,42,43]. The detailed synthetic procedure is presented in Supplementary Material Section 2).

### 2.2. Powder X-Ray Diffraction (PXRD)

X-ray powder diagrams were obtained with an Empyrean diffractometer equipped with a Pixel 3D detector,  $\text{CuK}\alpha$  radiation source ( $\lambda = 1.5418 \text{ \AA}$ ) 40 mA, 40 kV. The best counting statistics were achieved using a scanning step of  $0.05^\circ$  between  $5^\circ$  and  $40^\circ$  Bragg angles with an exposure time of 5 s per step. The PXRD of all powdered samples were compared with the respective simulated patterns and showed in Supplementary Material Section 3. The structure conservation of the sensors after thermal treatment and toxics expositions were also analyzed by PXRD (see Supplementary Material Section 4).

### 2.3. Thermal Analysis

Thermogravimetric analysis (TGA) and differential thermal analysis (DTA) were simultaneously performed with Shimadzu TGA-51, DTA-50 apparatus (Shimadzu, Japan) under flowing air at a flow rate of  $50 \text{ mL min}^{-1}$  and a heating rate of  $10 \text{ }^\circ\text{C min}^{-1}$ . Vibrational spectroscopy and thermal analysis were carried out in order to check the reported formula (Supplementary Material Section 5).

#### 2.4. Fourier Transform Infrared Spectroscopy (FTIR)

FTIR spectra were recorded with a Nicolet Protégé 460 spectrometer in the range 4000–600  $\text{cm}^{-1}$ ; spectra were recorded averaging 64 scans and with a spectral resolution of 4  $\text{cm}^{-1}$  by the KBr pellet technique.

#### 2.5. Scanning Electron Microscopy (SEM) and Energy-Dispersive X-ray Spectra (EDS)

Crystal morphology and EDS semiquantitative analysis were performed on an FEI Quanta 400 microscope.

#### 2.6. UV Absorption Spectroscopy

UV Absorption Spectra of Analytes were Recorded with a UV Spectrophotometer-160A (Shimadzu, Japan).

#### 2.7. Luminescence Measurements

For sensing measurements, suspensions containing 1.5 mg of the activated MOF (for **Eu-BPDC** and **Eu-BTC**) in 3 mL of the methanolic solutions were ultrasonicated for 30 min in a Clausius apparatus for an efficient analyte-sensor contact. For sensor activation procedures, see Supplementary Material Sections 4–6. The measurements were carried out in a Félix X32 PTI spectrofluorometer with Xe UXL-75 Xe lamp employing a quartz cell of 1 cm of optical path (Horiba, Japan). The chosen excitation wavelengths were 393 nm and 352 nm for Eu-MOFs and Tb-MOFs, respectively. The monitored 4f–4f hypersensitive transitions for  $\text{Eu}^{3+}$  and  $\text{Tb}^{3+}$  were  ${}^5\text{D}_0 \rightarrow {}^7\text{F}_2$  (615 nm) and  ${}^5\text{D}_4 \rightarrow {}^7\text{F}_5$  (541 nm).

#### 2.8. Simulation Details

System setup: Classical MD simulations reported in this paper were performed using the Amber16 program suite [44]. The all-atoms system was represented by the general AMBER force field (GAFF) set of parameters, while the europium parameters were published elsewhere [45–47]. Partial atomic charges were calculated by the AM1BCC method [48,49] using the antechamber set of auxiliary programs [44].

The atomistic description of the host frameworks was constructed from the experimental crystallographic data taken from previous studies [45–47]. A supercell representation having  $3 \times 3 \times 3$  primitive cells was sufficient in our case to allow us to embed the guest molecules and obtain reliable results. The supercell representations account for  $\sim 100\text{\AA}$ ,  $\sim 60\text{\AA}$ , and  $\sim 58\text{\AA}$  in the X, Y, and Z directions, respectively.

The molecular structure of the guest molecules, namely metsulfuron (**MSM**; IUPAC: 2-[(4-methoxy-6-methyl-1,3,5-triazin-2-yl)amino]oxomethylsulfamoyl]benzoic acid methyl ester), imazalil (**IMZ**; IUPAC: 1-[2-(2,4-dichlorophenyl)-2-[(prop-2-en-1-yl)oxy]ethyl]-1H-imidazole), chlorimuron (**CLM**; IUPAC: ethyl 2-[(4-chloro-6-methoxypyrimidin-2-yl)carbamoysulfamoyl]benzoate), and chlorpyrifos (**CLP**; IUPAC: O,O-Diethyl O-3,5,6-trichloropyridin-2-yl phosphorothioate), were built from coordinates published elsewhere [50–53].

A molecular representation of the pesticides is displayed in Figure 1. Four pores within the host framework were used to confine a single representation of each guest molecule in the inside of the pore. Afterwards, the whole system was immersed in a cubic methanol box with 15  $\text{\AA}$  buffer regions. The final model system (i.e., guests: host framework: methanol box) contained  $\sim 16,962$  total atoms and an approximated dimension of  $\sim 166\text{\AA}$ ,  $\sim 127\text{\AA}$ , and  $\sim 127\text{\AA}$  in the X, Y, and Z directions respectively. The model system had its coordinates optimized and energy minimized for 10,000 steps of the steepest descendent and then equilibrated at 298 K and 1 atm in the NPT (constant number of particles (N), pressure (P), and temperature (T); T is regulated via a thermostat, which typically adds a degree of freedom to the conserved Hamiltonian) ensemble holding of the host framework as a rigid body. For a constant temperature and pressure regulation, the Berendsen thermostat and

barostat were used [54]. Finally, 60 ns of production run were performed in the NVT (constant number of particles (N), volume (V), and temperature (T); T is regulated via a thermostat, which typically adds a degree of freedom to the conserved Hamiltonian) ensemble. A time step of 4 fs was used for all the simulations due to the hydrogen mass repartitioning [55] the whole model system. The particle mesh Ewald (PME) algorithm [56] together with the periodic boundary condition (PBC) was employed throughout the simulations with a 8 Å non-bonded cut-off. Snapshots were saved every 5 ps, which produced 12,000 snapshots in total for each guest molecule.

Post-processing: The saved snapshots were postprocessed to quantify the Eu:X (X = N,O,S) contacts by using the AmberTools set of auxiliary programs [44]. The stability of the contact is reflected by the fraction of contact preserved over the analyzed set of snapshots. The most stable contacts will tend to be formed within the selected cutoff of 3 Å during most of the analyzed set of snapshots, and they will show during a bigger fraction of time.

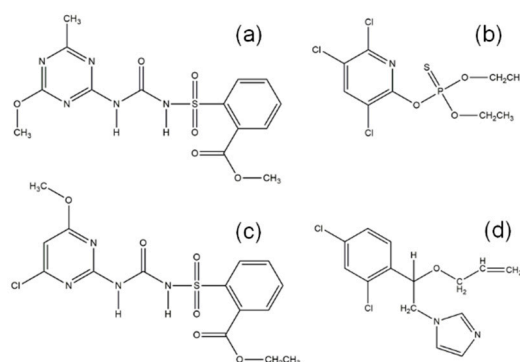


**Figure 1.** Molecular representation of the pesticides and herbicides used in this work: **MSM** (metsulfuron) (a), **CLP** (chlorpyrifos) (b), **CLM** (chlorimuron) (c) **IMZ** (imazalil) (d).

### 3. Results and Discussion

#### 3.1. Synthesis of Luminescent MOFs Sensors

The described synthetic procedures in Supplementary Material Section 2 led to crystalline products (Figure 2), which were fully characterized by PXRD, TGA-DSC, and FTIR.

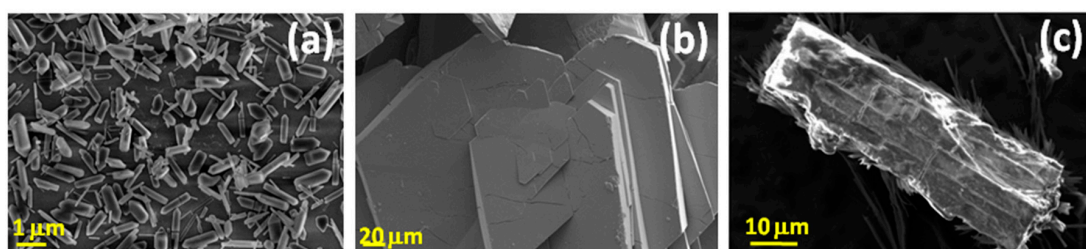


**Figure 2.** SEM micrographs of **Eu-BTC** (a) and **Eu-PSA** (b) crystalline materials. **Eu-BTC** “block” crystal after **MSM** exposition (c).

**Eu-BPDC** corresponds to a 3D structure compound which crystallizes into the monoclinic  $C2/c$  space group, where the asymmetric unit contains one seven-coordinated europium ion, one-and-a-half BPDC ligands, and one coordinated water molecule (see Figure 3). Each lanthanide atom is bridged by four BPDC groups, giving rise to paddle-wheel building blocks. The paddle-wheel building blocks connect each other through two carboxyl groups along the  $[0\ 0\ 1]$  direction, leading to a one-dimensional (1D) inorganic chain. These chains are linked through biphenyl groups forming the 3D framework. According to the calculations of cavity volume, the 3D framework contains  $25.2\ \text{Å} \times 17.1\ \text{Å}$  nanochannels along the diagonals (see Figure 3).



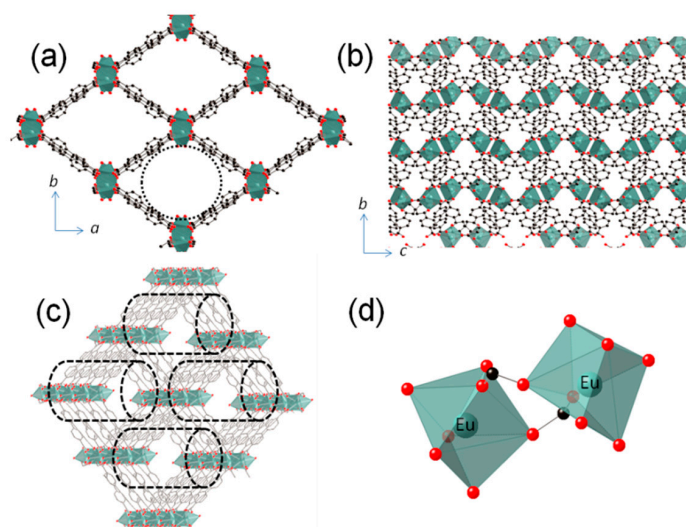


**Figure 3.** Projection on the *ab* and *bc* planes of **Eu-BPDC** (a,b), and the view of the nanochannels in the structure (c). The lanthanide environment of two adjacent metallic centers (d). Hydrogen atoms were omitted for clarity.

For the case of **Eu-BTC**, the structure is 3D belonging to tetragonal  $P4_322$  space group. Each asymmetric unit is composed of one seven-coordinated europium ion, one BTC linker, and one water molecule. Each lanthanide ion is surrounded by six oxygen atoms from six carboxylate groups of BTC and one oxygen atom from a terminal water molecule. The metallic chain polyhedra are developed in a helical fashion along the *c* axis, chains which are linked by BTC ligands along the *a* and *b* axis, giving rise to a 3D framework (see Figure 4). The structure contains unidimensional channels along the *c* direction, with a circular area of  $36 \text{ \AA}^2$ . Both **Eu-BPDC** and **Eu-BTC** can be described as polyhedra chains connected by ligands in two directions, conforming to a 3D framework.

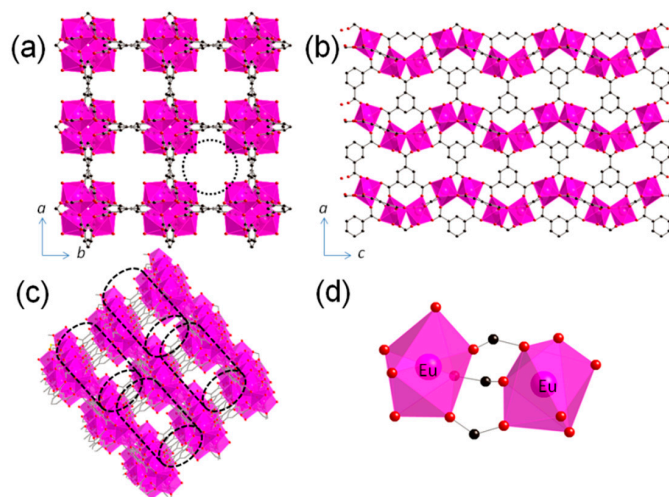


**Figure 4.** Projection on the *ab* and *ac* planes of **Eu-BTC** (a,b), and the view of the nanochannels in the structure (c). The lanthanide environment of two adjacent metallic centers (d). Hydrogen atoms were omitted for clarity.

Finally, **Eu-PSA** can be described as a layered structure (monoclinic  $P2_1/c$  space group) where the asymmetric unit is composed by two crystallographic independent europium ions with coordination numbers of 8 and 9 respectively. As can be seen in Figure 5, the framework can be described as polyhedra chains along the *c* direction connected by PSA ligands. As it was previously analyzed [42],

no free voids were found in this structure, and this fact was a sufficient reason to classify this compound as a CP and not as MOF.

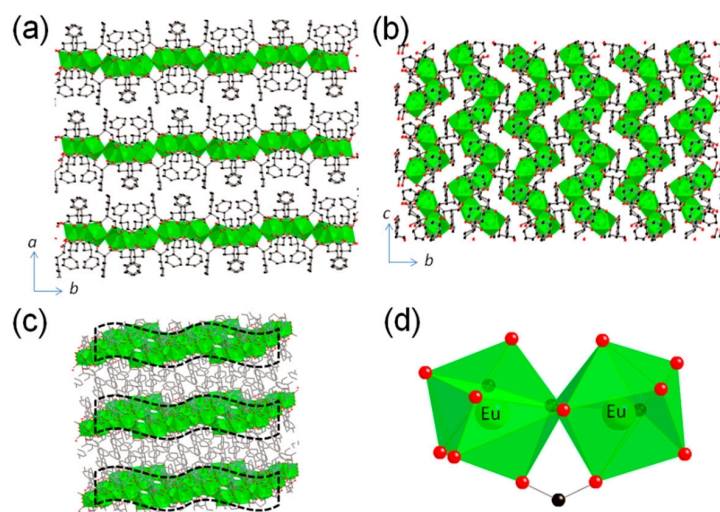


**Figure 5.** Projection on the *ab* and *bc* planes of **Eu-PSA** (a,b), and the development of the layered structure (c). The lanthanide environment of two adjacent metallic centers (d). Hydrogen atoms were omitted for clarity.

### 3.2. Sensing Essays

The optically active phases **Eu-PSA**, **Tb-PSA**, **Eu-BTC**, and **Eu-BPDC** were selected as chemosensing platforms. According to Figure 6; Figure 7, in the 2D **Eu-PSA** and **Tb-PSA** compounds, the electroaffinity of transition metal ions such as  $\text{Cu}^{2+}$ ,  $\text{Mn}^{2+}$ , and  $\text{UO}_2^{2+}$  justified the attenuation of quenching luminescence [38,39]. On the other hand, the quenching of 4f transitions through the organic species can be explained by electroaffinity behavior exhibited by the analytes.

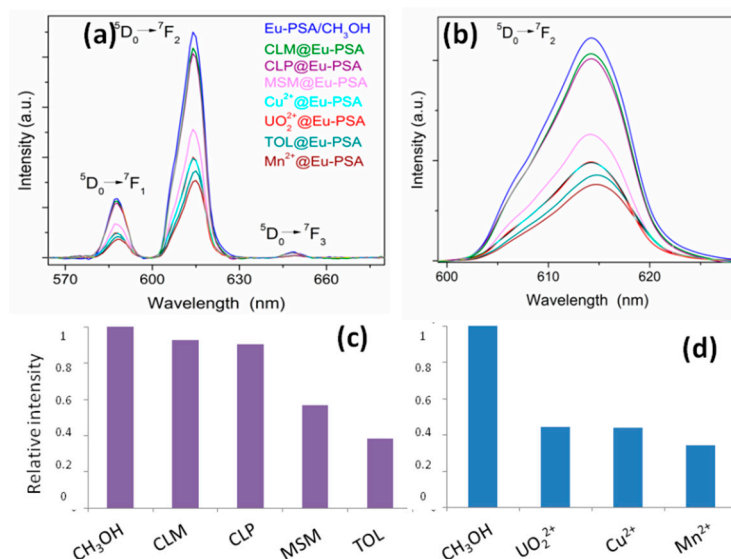


**Figure 6.** (a) Emission spectra of **Eu-PSA** under diverse pollutant exposition (concentration =  $2 \times 10^{-3}$  M). (b) Zoomed region of the  $\text{Eu}^{3+}$  hypersensitive  ${}^5\text{D}_0 \rightarrow {}^7\text{F}_2$  transition. (c) Relative intensities of the hypersensitive signal of **Eu-PSA** (down) in the presence of organic and (d) inorganic pollutants.

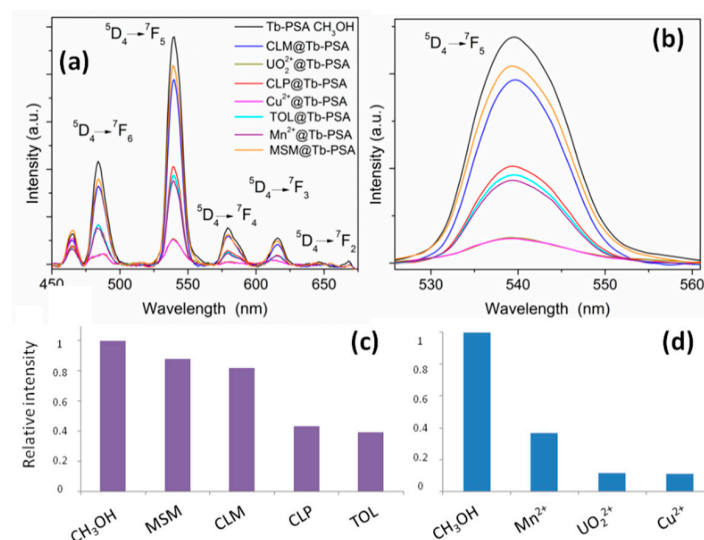


**Figure 7.** (a) Emission spectra of **Tb-PSA** under excitation to different pollutants (concentration =  $2 \times 10^{-3}$  M). (b) Zoomed region of the **Tb<sup>3+</sup>** hypersensitive  $^5D_4 \rightarrow ^7F_5$  transition. Relative intensities of the hypersensitive signal of **Tb-PSA** in the presence of organic (c) and inorganic (d) pollutants.

The quenching efficiency (QE) can be defined as:  $QE\% = (I_0 - I)/I_0 \times 100$ , where  $I_0$  and  $I$  represent the emission intensity values in the absence and in the presence of the analytes at the same concentration ( $2 \times 10^{-3}$  M), respectively. Based on these results,  $Cu^{2+}$  and  $[UO_2]^{2+}$  cationic species represent efficient quenchers for the luminescence of **Tb-PSA**, exhibiting a QE of 89%. Regarding the organic molecules, CLP exhibits a QE% of 60%, a value comparable to that of toluene (TOL) (Figure 8). As shown in Supplementary Material Section 8, these analytes show UV absorption bands ranging from 200 to 350 nm. The absorption peak of the ligand within **Eu-PSA** (or **Tb-PSA**) is overlapped by the absorbing range of the toxics, which implies that a competition of the excitation energy between the organic linker (PSA) and the analytes takes place. The majority of the toxics absorb most of the energy, and only a small fraction of energy will be transferred through the ligand to the **Tb<sup>3+</sup>** or **Eu<sup>3+</sup>** ions. This also illustrates why other pollutant molecules present similar quenching effects on the luminescence intensity of **Tb-PSA** and **Eu-PSA**.

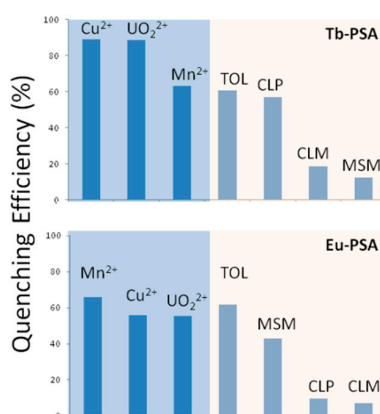


**Figure 8.** QE% of compounds **Tb-PSA** (above) and **Eu-PSA** (below) in the presence of different pollutants.

With the purpose of evaluating the inorganic pollutant concentration effect on the PL intensity of **Tb-PSA**, two cationic species of environmental relevance and high QE were chosen ( $Cu^{2+}$  and  $[UO_2]^{2+}$ ). Figure 9 shows that a gradual increase in the uranyl concentration produced a decrease in the  $^5D_4 \rightarrow ^7F_5$  hypersensitive signal with an intensity quenching of 94% at a maximum  $[UO_2]^{2+}$  concentration of 4000 ppm. The relative intensity decreases markedly with the uranyl concentration, following a



biexponential behavior. This suggests that uranyl species can intervene in at least two main radiative transition paths after excitation. In a first approximation, the effect of uranyl in the fluorescence quenching processes was modeled according to the Stern–Volmer law, [57]  $I_0/I = 1 + K_{SV} \times [UO_2]^{2+}$ . In this equation,  $I_0$  and  $I$  are the luminescent intensities of the  ${}^5D_4 \rightarrow {}^7F_5$  transition of **Tb-PSA** before and after being exposed to different concentrations of  $[UO_2]^{2+}$  respectively,  $K_{SV}$  being the quenching coefficient (see the graphics in Supplementary Material Sections 9 and 10). An equivalent study for  $Cu^{2+}$  ions in the range 0–2340 ppm leads to similar responses (see Figure 10). In both cases, the correlation obtained in the quenching effect is not completely linear. This effect is more marked at higher copper(II) or uranyl concentrations, reflecting multiple interactions between the ions and the MOF matrices. We can speculate that the observed biexponential intensity decay with increasing metal concentration can reflect multiple ion–MOF interactions, such as adsorption in different surface sites or remote energy transfer. However, in the lower concentration range, the agreement with the Stern–Volmer model is far better, supporting that a quenching process of diffusional nature takes place in dilute solutions. These observations support the fact that the bidimensional architectures **Tb-PSA** and **Eu-PSA** are closed to guest analytes; therefore, only superficial dynamic quenching can take place in these compounds. In addition, these experiments demonstrate the potential of detecting cationic species by quenching at low concentrations. The limit of detection (LOD) of the proposed method employing **Tb-PSA** was calculated to be 2.9 ppm for  $[UO_2]^{2+}$  and 5.6 ppm for  $[Cu^{2+}]$ . Note that LOD is defined by the equation  $LOD = 3S_0/K$ , where  $S_0$  is the standard deviation of blank measurements ( $n = 10$ ) and  $K$  is the slope of the calibration curve. An in-depth analysis is in progress in order to compare the MOF architectures with respect to analytical performance in parameters such as sensitivity and selectivity, which will be reported in a forthcoming paper.

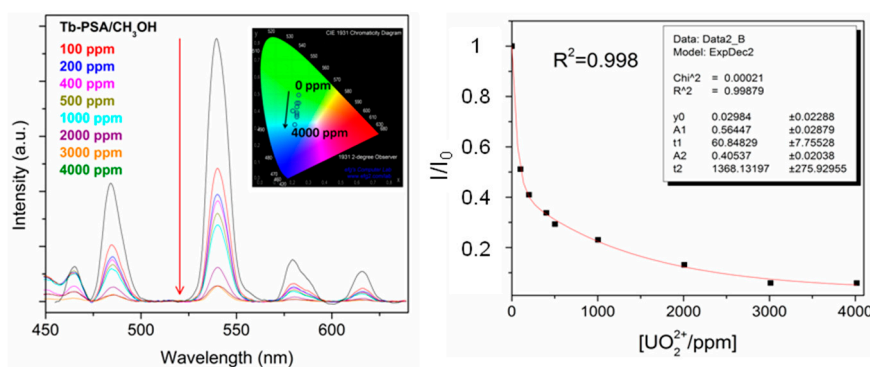


**Figure 9.** Left: Emission spectra and Commission Internationale de l'Éclairage (CIE x,y) chromaticities of **Tb-PSA** from 0 to 4000 ppm of  $[UO_2]^{2+}$  (inset). Right: Relative intensity ( $I/I_0$ ) of the  $Tb^{3+}$  hypersensitive transition.

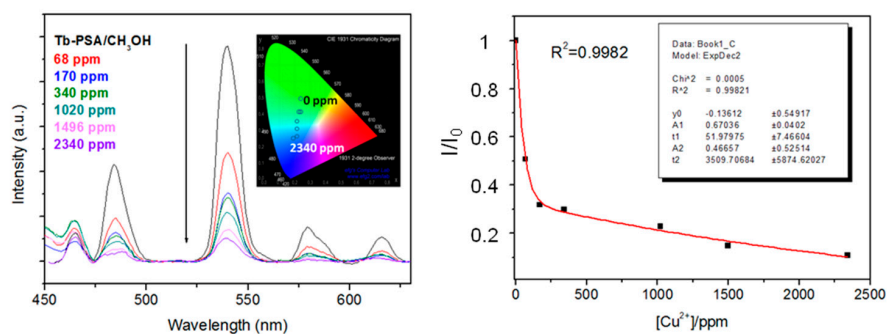


**Figure 10.** Left: Emission spectra and CIE x,y chromaticities of **Tb-PSA** from 0 to 2340 ppm of  $Cu^{2+}$ . Right: Relative intensity ( $I/I_0$ ) of the  $Tb^{3+}$  hypersensitive transition.

In the case of 3D porous MOFs, thermal activation was made prior to the sensing studies in order to release DMF molecules from the pores, thus freeing the cavities for sensing essays. In order to study the influence of the thermal activation on the sensing performance, the luminescent properties of **Eu-BTC** and the corresponding activated material (**Eu-BTC'**) were evaluated. The BET surface area exhibited for **Eu-BTC'** ( $458 \text{ m}^2 \cdot \text{g}^{-1}$ ) confirmed its potential properties as molecule–guest material. The corresponding nitrogen isotherm curve for **Eu-BTC'** (measured at 77 K) is shown in Supplementary Material Section 11. According to the results, **Eu-BTC** exhibited a marked quenching when it was contacted with MSM and cationic species as it was seen in 2D frameworks (Figure 11). Nevertheless, an intensity enhancement is identified when **Eu-BTC** is in contact with TOL, CLP, CLM, and IMZ. The differential optical behavior of **Eu-BTC** makes the MOF a potential specific sensor of toxic pollutants. We can hypothesize that the increase in the intensity is due to the energetic transfer from the analytes to the lanthanide ions provided by the “confinement effect” of the porous sensor. In addition, the thermal activation significantly improved the sensitivity, which is reflected when the  $^5\text{D}_0 \rightarrow ^7\text{F}_2$  intensities of activated and nonactivated **Eu-BTC** are compared (Figure 12). Moreover, QE% of **Eu-BTC'** in the presence of CLP,  $[\text{UO}_2]^{2+}$ , and  $\text{Cu}^{2+}$  was determined as 50, 72, and 27% respectively, demonstrating a sensitization of  $\text{Eu}^{3+}$  towards the uranyl cations. In this sense, when MSM interacted with the activated material, the hypersensitive signal was sixteen times more intense than the one observed on the nonactivated compound. It seems that MSM acts as a quencher in the solvent-containing phase, but an improved analyte–matrix interaction produces an extra enhancement in the corresponding transition.

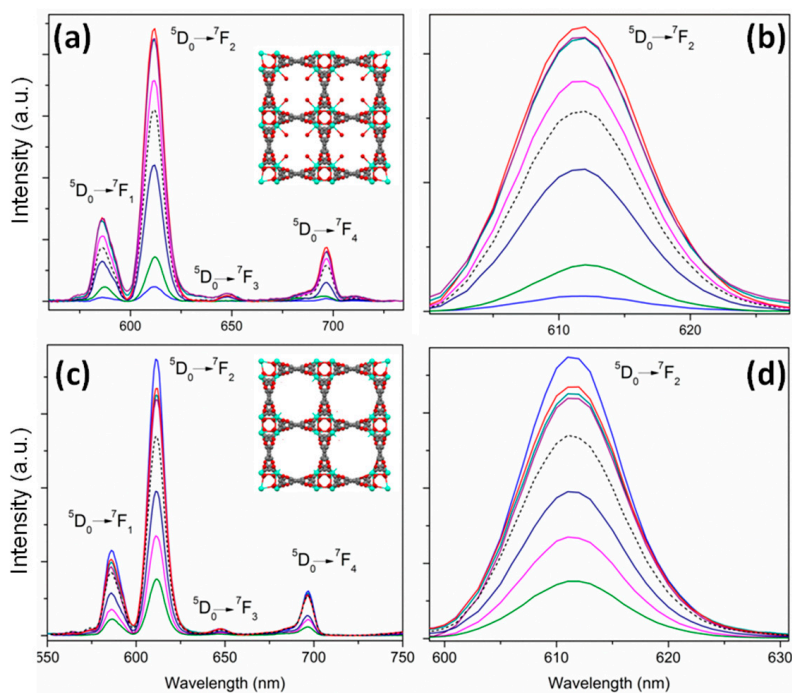


**Figure 11.** Emission spectra of **X@Eu-BTC** (a) and **X@Eu-BTC'** (c) under diverse pollutant exposition (blue: **MSM**; purple: **CLM**; pink: **CLP**; red: **TOL**; dark yellow: **IMZ**; olive:  $\text{UO}_2^{2+}$ ; deep-blue:  $\text{Cu}^{2+}$ ) (a). Black dashed line spectra correspond to those of **Eu-BTC** and **Eu-BTC'** in methanol without analyte species. Zoomed region of the  $\text{Eu}^{3+}$  hypersensitive  $^5\text{D}_0 \rightarrow ^7\text{F}_2$  transition (b,d).

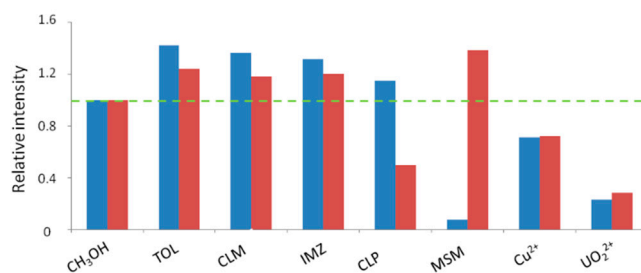


**Figure 12.**  ${}^5D_0 \rightarrow {}^7F_2$  intensities of  $X@Eu-BTC$  (blue) and  $X@Eu-BTC'$  (red). The dashed green line denotes the systems without analyte presence.

In the same vein, a more intimate interaction between **Eu-BPDC'** and the analytes is observed, where the hypersensitive transition suffered remarkable intensity and shape band changes mainly in  ${}^5D_0 \rightarrow {}^7F_2$  and  ${}^5D_0 \rightarrow {}^7F_4$  transitions (Figure 13a,b). In comparison with the other open framework **Eu-BTC'**, the same tendency was observed when the **Eu-BPDC'** sensor was contacted with uranyl, showing a quenching of 78% (Figure 13c).

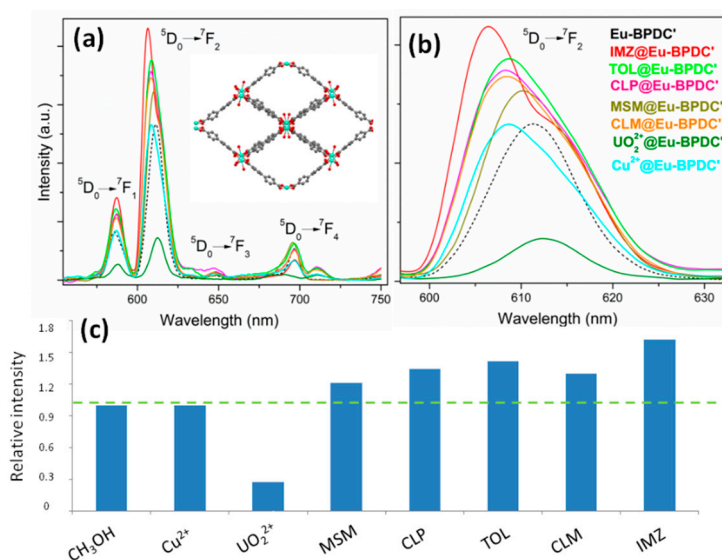


**Figure 13.** (a) Emission spectra of  $X@Eu-BPDC'$  exposed to diverse pollutants (X). (b) Zoomed region of the  $Eu^{3+}$  hypersensitive  ${}^5D_0 \rightarrow {}^7F_2$  transition. (c) Relative intensities of the hypersensitive signal of **Eu-BPDC'** in the presence of diverse pollutants, of  $X@Eu-BPDC'$ ; the dashed green line denotes the system without analyte presence.

### 3.3. Sensor–Analyte Interaction Studies

In the previous sections, a variety of optical responses was observed, which depended on the pore structure and type of interactions with the MOF matrix. In order to gain a more complete description of sensor–analyte interactions, simulations were carried out. The vibrational analysis was focused particularly on the porous **Eu-BPDC** and **Eu-BTC**, since the process of thermal activation led to stable frameworks with permanent porosity suitable for host–guest interactions assays. As stated above, no activation was necessary for **Eu-PSA** due to its layered structure, with no free voids for host–guest interactions. In addition, the luminescence studies showed that the layered phases exhibited a diffusional quenching, but a more complex and intimate interaction of the analytes took place with the porous frameworks. For this in-depth study of the contact efficiency of  $X@Eu-MOF$  systems involving vibrational analysis, the sensors **Eu-BTC** and **Eu-BPDC** were chosen for simplicity. A more detailed description can be found in Supplementary Material Section 12. The model system of host–guest interaction constructed employing the Amber software is depicted in Figure 14.

In light of all the results, we can state that the different sensing behavior observed is mainly due to the structure framework topology, making possible the quenching of luminescence through energy transfers between the lanthanide centers and the analytes (pesticides and cations) in the layered compounds. In addition, for open frameworks, a “confinement effect” was anticipated and a “host–guest” interaction was confirmed by a combinatorial vibrational-theoretical approach. For this reason, a mechanism involving energy transfers with quenching and enhancements of luminescent signals can be proposed in principle. Both mechanisms are outlined in Scheme 1.

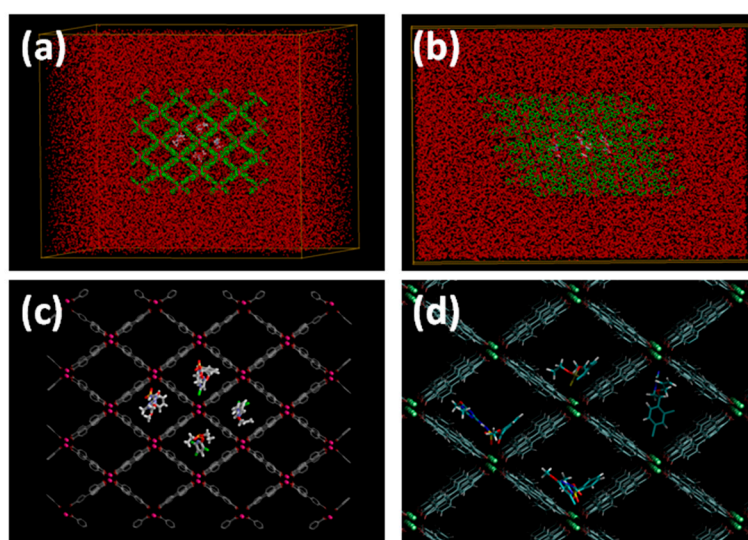
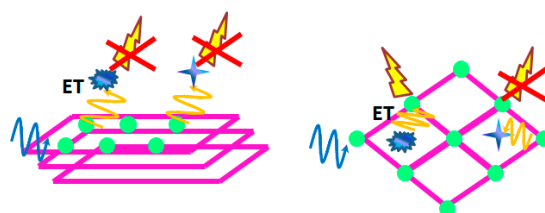


**Figure 14.** Model system of host–guest interaction (a,b) with supercell dimensions of  $166 \text{ \AA} \times 127 \text{ \AA} \times 127 \text{ \AA}$  (total atoms number: 16,962) constructed by Amber program. Zoom of the pesticides and herbicides into the metal organic frameworks (MOF) (c,d) (MOF dimensions (x,y,z):  $100 \text{ \AA} \times 60 \text{ \AA} \times 58 \text{ \AA}$ ).



**Scheme 1.** Diverse mechanisms proposed to take place in 2D Ln-PSA and 3D Eu-BPDC and Eu-BTC.

#### 4. Conclusions

A set of luminescent MOFs (LMOFs) based on lanthanides have been hydrothermally obtained, fully characterized, and used as potential chemosensors towards pesticides and cations. The hypersensitive transitions of  $^5D_0 \rightarrow ^7F_2$   $\text{Eu}^{3+}$  and  $^5D_4 \rightarrow ^7F_5$   $\text{Tb}^{3+}$  ions were employed to detect analytes by analyzing variations of the fluorescence intensity ratio ( $I/I_0$ ). In the case of layered coordination polymer frameworks (Ln-PSA), a quenching of luminescence was noticeable in the presence of cations and pesticides, which can be explained by a diffusional fluorescence quenching. This phenomenon was successfully understood in terms of the Stern–Volmer law. On the other hand, the open frameworks (Eu-BTC and Eu-BPDC) exhibited preferential quenching in the presence of paramagnetic cations, while an interaction with aromatic pesticides contributes to an enhancement in the fluorescent signal due to their rich electron nature. It is important to remark that these results are the first reports of uranyl species and pesticide sensing using MOF platforms.

Finally, the host–guest interaction of the open frameworks was studied in terms of vibrational analysis. The dynamic simulations support the hypothesis of the importance of the interactions and confinement between the sensor and the pesticides. These results open up the potential applications of

MOFs for sensing toxins of environmental interest, as well as the development of optical devices for analytical chemistry.

**Supplementary Materials:** The following are available online at <http://www.mdpi.com/1424-8220/19/5/1260/s1>.

**Author Contributions:** Conceptualization, G.E.G. and G.J.A.A.S.-I.; Data curation, G.E.G., M.d.S.A., H.A.B. and F.R.; Formal analysis, G.E.G., M.d.S.A., F.R. and G.J.A.A.S.-I.; Investigation, G.E.G., M.d.S.A., H.A.B., F.R. and G.J.A.A.S.-I.; Methodology, G.E.G. and M.d.S.A.; Supervision, G.J.A.A.S.-I.; Visualization, H.A.B.; Writing—original draft, G.E.G.; Writing—review & editing, G.E.G., M.d.S.A., H.A.B., F.R. and G.J.A.A.S.-I.

**Funding:** This work was supported by the Consejo Nacional de Investigaciones Científicas y Técnicas (PIP CONICET 2012-2087) and ANPCyT (PICT 2014-3687, 2016-3017 and 2015-3526). G.E.G. acknowledges a post-doctoral CONICET fellowship.

**Acknowledgments:** G.E.G., F.R., H.A.B. and G.J.A.A.S.-I. are members of CIC-CONICET. Authors want to thank Cristian Lillo for valuable discussions.

**Conflicts of Interest:** The authors declare no conflict of interest.

## References

1. Li, J.-R.; Sculley, J.; Zhou, H.-C. Metal–organic frameworks for separations. *Chem. Rev.* **2012**, *112*, 869–932. [[CrossRef](#)] [[PubMed](#)]
2. Gomez, G.E.; Brusau, E.V.; Sacanell, J.; Sacanell, G.J.A.A.; Narda, G.E. Insight into the metal content–structure–property relationship in lanthanide metal–organic frameworks: Optical studies, magnetism, and catalytic performance. *Eur. J. Inorg. Chem.* **2018**, *20–21*, 2452–2460. [[CrossRef](#)]
3. Gomez, G.E.; Gomez, R.F.; Lionello, D.F.; Aguirre-Díaz, L.M.; Spinosa, M.; Costa, C.S.; Fuertes, M.C.; Pizarro, R.A.; Kaczmarek, A.M.; Ellena, J.; et al. Exploring physical and chemical properties in new multifunctional indium-, bismuth-, and zinc-based 1d and 2d coordination polymers. *Dalton Trans.* **2018**, *47*, 1808–1818. [[CrossRef](#)] [[PubMed](#)]
4. Dalton, A.; García, H.; Llabrés, F.X. I xamena. engineering metal organic frameworks for heterogeneous catalysis. *Chem. Rev.* **2010**, *110*, 4606–4655.
5. Dhakshinamoorthy, A.; Li, Z.; Garcia, H. Catalysis and photocatalysis by metal organic frameworks. *Chem. Soc. Rev.* **2018**, *47*, 8134–8172. [[CrossRef](#)] [[PubMed](#)]
6. Bünzli, J.-C.G.; Comby, S.; Chauvin, A.-S.; Vandevyver, C.D.B. New opportunities for lanthanide luminescence. *J. Rare Earths* **2007**, *25*, 257–274. [[CrossRef](#)]
7. Le Natur, F.; Calvez, G.; Daiguebonne, C.; Guillou, O.; Bernot, K.; Ledoux, J.; le Pollès, L.; Roiland, C. Coordination polymers based on heterohexanuclear rare Earth complexes: Toward independent luminescence brightness and color tuning. *Inorg. Chem.* **2013**, *52*, 6720–6730. [[CrossRef](#)] [[PubMed](#)]
8. Fan, X.; Freslon, S.; Daiguebonne, C.; Calvez, G.; le Pollès, L.; Bernot, K.; Guillou, O. Heteronuclear lanthanide-based coordination polymers exhibiting tunable multiple emission spectra. *J. Mater. Chem. C* **2014**, *2*, 5510–5525. [[CrossRef](#)]
9. Werts, M.H.V. Making sense of lanthanide luminescence. *Sci. Prog.* **2005**, *88*, 101–131. [[CrossRef](#)]
10. Marling, J. 1.05–1.44  $\mu\text{m}$  tunability and performance of the CW Nd<sup>3+</sup>: YAG laser. *IEEE J. Sel. Top. Quantum Electron.* **1978**, *14*, 56–62. [[CrossRef](#)]
11. Polman, A.; van Veggel, F.C.J.M. Veggel. Broadband sensitizers for erbium-doped planar optical amplifiers: Review. *J. Opt. Soc. Am. B* **2004**, *21*, 871–892. [[CrossRef](#)]
12. D’Andrade, B.W.; Forrest, S.R. White organic light-emitting devices for solid-state lighting. *Adv. Mater.* **2004**, *16*, 1585–1595. [[CrossRef](#)]
13. Su, H.C.; Chen, H.F.; Fang, F.C.; Liu, C.C.; Wu, C.C.; Wong, K.T.; Liu, Y.H.; Peng, S.M. Solid-state white light-emitting electrochemical cells using iridium-based cationic Transition metal complexes. *J. Am. Chem. Soc.* **2008**, *130*, 3413–3419. [[CrossRef](#)] [[PubMed](#)]
14. Niu, Y.H.; Liu, M.S.; Ka, J.W.; Bardker, J.; Zin, M.T.; Schofield, R.; Chi, Y.; Jen, A.K.Y. Crosslinkable hole-transport layer on conducting polymer for high-efficiency white polymer light-emitting diodes. *Adv. Mater.* **2007**, *19*, 300–304. [[CrossRef](#)]
15. Bünzli, J.-C.G.; Piguët, C. Taking advantage of luminescent lanthanide ions. *Chem. Soc. Rev.* **2005**, *34*, 1048–1077. [[CrossRef](#)] [[PubMed](#)]



16. Brites, C.D.S.; Lima, P.P.; Silva, N.J.O.; Millán, A.; Amaral, V.S.; Palacio, F.; Carlos, L.D. Lanthanide-based luminescent molecular thermometers. *New J. Chem.* **2011**, *35*, 1177–1183. [[CrossRef](#)]
17. Ananias, D.; Brites, C.D.S.; Carlos, L.D.; Rocha, J. Cryogenic nanothermometer based on the MIL-103 (Tb,Eu) metal-organic framework. *Eur. J. Inorg. Chem.* **2016**, *13–14*, 1967–1971. [[CrossRef](#)]
18. Hu, Z.; Deibert, B.J.; Li, J. Luminescent metal-organic frameworks for chemical sensing and explosive detection. *Chem. Soc. Rev.* **2014**, *43*, 5815–5840. [[CrossRef](#)]
19. Bernini, M.C.; Gomez, G.E.; Brusau, E.V.; Narda, E.G. Reviewing rare earth succinate frameworks from the reticular chemistry point of view: Structures, nets, catalytic and photoluminescence applications. *Israel J. Chem.* **2018**, *58*, 1044–1061. [[CrossRef](#)]
20. Gomez, G.E.; Bernini, M.C.; Brusau, E.V.; Narda, G.E.; Massad, W.A.; Labrador, A. two sets of metal organic frameworks along the lanthanide series constructed by 2,3-dimethylsuccinate: Structures, topologies, and strong emission without ligand sensitization. *Cryst. Growth Des.* **2013**, *13*, 5249–5260. [[CrossRef](#)]
21. Lin, Z.-J.; Lü, J.; Hong, M.; Cao, R. Metal-organic frameworks based on flexible ligands (FL-MOFs): Structures and applications. *Chem. Soc. Rev.* **2014**, *43*, 5867–5895. [[CrossRef](#)]
22. Chen, B.; Wang, L.; Zapata, F.; Qian, G.; Lobkovsky, E.B.A. luminescent microporous metal-organic framework for the recognition and sensing of anions. *J. Am. Chem. Soc.* **2008**, *130*, 6718–6719. [[CrossRef](#)]
23. Chen, B.; Yang, Y.; Zapata, F.; Lin, G.; Qian, G.; Lobkovsky, E.B. Luminescent open metal sites within a metal-organic framework for sensing small molecules. *Adv. Mater.* **2007**, *19*, 1693–1696. [[CrossRef](#)]
24. Guo, X.; Zhu, G.; Fang, Q.; Xue, M.; Tian, G.; Sun, J.; Li, X.; Qiu, S. Synthesis, structure and luminescent properties of rare earth coordination polymers constructed from paddle-wheel building blocks. *Inorg. Chem.* **2005**, *44*, 3850–3855. [[CrossRef](#)]
25. Chen, T.; Huo, P.; Hou, J.-L.; Xu, Q.-Z.; Dai, J. Confinement effects of metal-organic framework on the formation of charge-transfer tetrathiafulvalene dimers. *Inorg. Chem.* **2016**, *55*, 12758–12765. [[CrossRef](#)]
26. Gomez, G.E.; Brusau, E.V.; Kaczmarek, A.M.; Mellot-Draznieks, C.; Sacanell, J.; Rouse, G.; van Deun, R.; Sanchez, C.; Narda, G.E.; Illia, G.J.A.A.S. Flexible ligand-based lanthanide three-dimensional metal-organic frameworks with tunable solid-state photoluminescence and oh-solvent-sensing properties. *Eur. J. Inorg. Chem.* **2017**, *2017*, 2321–2331. [[CrossRef](#)]
27. Gomez, G.E.; Kaczmarek, A.M.; van Deun, R.; Brusau, E.V.; Narda, G.E.; Vega, D.; Iglesias, M.; Gutierrez-Puebla, E.; Monge, M.A. Photoluminescence, unconventional-range temperature sensing, and efficient catalytic activities of lanthanide metal-organic frameworks. *Eur. J. Inorg. Chem.* **2016**, *2016*, 1577–1588. [[CrossRef](#)]
28. D’Vries, R.F.; Gomez, G.E.; Lionello, D.F.; Fuertes, M.C.; Soler-Illia, G.J.A.A.; Ellena, J. Luminescence chemical sensing and mechanical properties of crystalline materials based on lanthanide-sulfonate coordination polymers. *RSC Adv.* **2016**, *6*, 110171–110181. [[CrossRef](#)]
29. Godoy, A.A.; Gomez, G.E.; Kaczmarek, A.M.; van Deun, R.; Furlong, O.J.; Gándara, F.; Monge, M.A.; Bernini, M.C.; Narda, G.E. Sensing properties, energy transfer mechanism and tuneable particle size processing of luminescent two-dimensional rare earth coordination networks. *J. Mater. Chem. C* **2017**, *5*, 12409–12421. [[CrossRef](#)]
30. Lustig, W.P.; Mukherjee, S.; Rudd, N.D.; Desai, A.V.; Li, J.; Ghosh, S.K. Metal-organic frameworks: Functional luminescent and photonic materials for sensing applications. *Chem. Soc. Rev.* **2017**, *46*, 3242–3285. [[CrossRef](#)]
31. Nicolopoulou-Stamati, P.; Maipas, S.; Kotampasi, C.; Stamatis, P.; Hens, L. Chemical pesticides and human health: The urgent need for a new concept in agriculture. *Front. Public Health* **2016**, *4*, 148. [[CrossRef](#)]
32. Weisenburger, D.D. Human health effects of agrichemical use. *Hum. Patol.* **1993**, *24*, 571–576. [[CrossRef](#)]
33. Yang, J.-S.; Swager, T.M. Fluorescent porous polymer films as TNT chemosensors: Electronic and structural effects. *J. Am. Chem. Soc.* **1998**, *120*, 11864–11873. [[CrossRef](#)]
34. Toal, S.J.; Trogler, W.C. Polymer sensors for nitroaromatic explosives detection. *J. Mater. Chem.* **2006**, *16*, 2871–2883. [[CrossRef](#)]
35. Sanchez, J.C.; DiPasquale, A.G.; Rheingold, A.L.; Trogler, W.C. Synthesis, luminescence properties, and explosives sensing with 1,1-tetraphenylsilole- and 1, 1-silafluorene-vinylene polymers. *Chem. Mater.* **2007**, *19*, 6459–6470. [[CrossRef](#)]
36. Nagarkar, S.S.; Joarder, B.; Chaudhari, A.K.; Mukherjee, S.; Ghosh, S.K. Highly selective detection of nitro explosives by a luminescent metal-organic framework. *Angew. Chem. Int. Ed.* **2013**, *52*, 2881–2885. [[CrossRef](#)]
37. Thomas, S.W.; Joly, G.D.; Swager, T.M. Chemical sensors based on amplifying fluorescent conjugated polymers. *Chem. Rev.* **2007**, *107*, 1339–1386. [[CrossRef](#)]

38. Jayaramulu, K.; Narayanan, R.P.; George, S.J.; Maji, T.K. Luminescent microporous metal–organic framework with functional lewis basic sites on the pore surface: Specific sensing and removal of metal ions. *Inorg. Chem.* **2012**, *51*, 10089–10091. [[CrossRef](#)]
39. Ma, J.-X.; Huang, X.-F.; Song, X.-Q.; Liu, W.-S. Assembly of Framework-Isomeric 4 d–4 f Heterometallic Metal-Organic Frameworks with Neutral/Anionic Micropores and Guest-Tuned Luminescence Properties. *Chem. Eur. J.* **2013**, *19*, 3590–3595. [[CrossRef](#)]
40. Hu, Z.; Pramanik, S.; Tan, K.; Zheng, C.; Liu, W.; Zhang, X.; Chabal, Y.J.; Li, J. Selective, sensitive, and reversible detection of vapor-phase high explosives via two-dimensional mapping: A new strategy for MOF-based sensors. *Cryst. Growth Des.* **2013**, *13*, 4204–4207. [[CrossRef](#)]
41. Banerjee, D.; Hu, Z.; Pramanik, S.; Zhang, X.; Wang, H.; Li, J. Vapor phase detection of nitroaromatic and nitroaliphatic explosives by fluorescence active metal–organic frameworks. *CrystEngComm* **2013**, *15*, 9745–9750. [[CrossRef](#)]
42. Gomez, G.E.; Bernini, M.C.; Brusau, E.V.; Narda, G.E.; Vega, D.; Kaczmarek, A.M.; van Deun, R.; Nazarro, M. Layered exfoliable crystalline materials based on sm-, eu- and eu/gd-2-phenylsuccinate frameworks. crystal structures, topology and luminescence properties. *Dalton Trans.* **2015**, *44*, 3417–3429. [[CrossRef](#)]
43. Guo, X.; Zhu, G.; Li, Z.; Sun, F.; Yang, Z.; Qiu, S. A lanthanide metal–organic framework with high thermal stability and available Lewis-acid metal sites. *Chem. Commun.* **2006**, 3172–3174. [[CrossRef](#)]
44. Case, D.A.; Betz, R.M.; Cerutti, D.S.; Cheatham, T.E., III; Darden, T.A.; Duke, R.E.; Giese, T.J.; Gohlke, H.; Goetz, A.W.; Homeyer, N.; et al. AMBER 2016 Manual, University of California, San Francisco. Available online: [www.ambermd.org](http://www.ambermd.org).
45. Baaden, M.; Berny, F.; Wipff, G.; Madic, C. M<sup>3+</sup> Lanthanide Cation Solvation by Acetonitrile: The Role of Cation Size, Counterions, and Polarization Effects Investigated by Molecular Dynamics and Quantum Mechanical Simulations. *J. Phys. Chem. A* **2000**, *104*, 7659–7671. [[CrossRef](#)]
46. Troxler, L.; Baaden, M.; Böhmer, V.; Wipff, G. Complexation of M<sup>3+</sup> lanthanide cations by calix[4]arene-CMPO ligands: A molecular dynamics study in methanol solution and at a water/chloroform interface. *Supramol. Chem.* **2000**, *12*, 27–51. [[CrossRef](#)]
47. Baaden, M.; Burgard, M.; Boehme, C.; Wipff, G. Lanthanide cation binding to a phosphoryl-calix[4]arene: The importance of solvent and counterions investigated by molecular dynamics and quantum mechanical simulations. *Phys. Chem. Chem. Phys.* **2001**, *3*, 1317–1325. [[CrossRef](#)]
48. Jakalian, A.; Bush, B.L.; Jack, D.B.; Bayly, C.I. Fast, efficient generation of high-quality atomic charges. AM1-BCC model: I. Method. *J. Comput. Chem.* **2000**, *21*, 132–146. [[CrossRef](#)]
49. Jakalian, A.; Jack, D.B.; Bayly, C.I. Fast, efficient generation of high-quality atomic charges. AM1-BCC model: II. Parameterization and validation. *J. Comput. Chem.* **2002**, *23*, 1623–1641.
50. McCourt, J.A.; Pang, S.S.; Guddat, L.W.; Duggleby, R.G. Elucidating the Specificity of Binding of Sulfonylurea Herbicides to Acetohydroxyacid Synthase. *Biochemistry* **2005**, *44*, 2330–2338. [[CrossRef](#)]
51. Cheon, S.; Shin, Y.W.; Park, K.M.; Kim, J.; Kim, T.H. Imaza-lil: 1-[2-(2,4-dichloro-phen-yl)-2-(prop-2-en-yloxy eth-yl)]-1H-imidazole. *Acta Cryst. E* **2011**, *67*, 01459. [[CrossRef](#)]
52. Lu, C.; Li, F.-S.; Yu, D.-S.; Wei Yao, Y.-L. Ethyl 2-[N-[N-(4-chloro-6-methoxy-pyrimidin-2-yl) carbamoyl] sulfamoyl] benzoate. *Acta Cryst. E* **2008**, *64*, 01248. [[CrossRef](#)]
53. Baughman, R.G.; Jorgensen, S.K.; Jacobson, R.A. Crystal and molecular structure of organophosphorus insecticides. 10. Chlorpyrifos. *J. Agric. Food Chem.* **1978**, *26*, 576–580. [[CrossRef](#)]
54. Berendsen, H.J.C.; Postma, J.P.M.; van Gunsteren, W.F.; DiNola, A.; Haak, J.R. Molecular dynamics with coupling to an external bath. *J. Chem. Phys.* **1984**, *81*, 3684–3690. [[CrossRef](#)]
55. Hopkins, C.W.; le Grand, S.; Walker, R.C.; Roitberg, A.E. Long-time-step molecular dynamics through hydrogen mass repartitioning. *J. Chem. Theory Comput.* **2015**, *11*, 1864–1874. [[CrossRef](#)]
56. Darden, T.; York, D.; Pedersen, L.J. Particle mesh Ewald: An N - log(N) method for Ewald sums in large systems. *Chem. Phys.* **1993**, *98*, 10089–10092. [[CrossRef](#)]
57. Wu, P.; Wang, J.; Li, Y.; He, C.; Xie, Z.; Duan, C. Luminescent Sensing and Catalytic Performances of a Multifunctional Lanthanide-Organic Framework Comprising a Triphenylamine Moiety. *Adv. Funct. Mater.* **2011**, *21*, 2788–2794. [[CrossRef](#)]



© 2019 by the authors. Licensee MDPI, Basel, Switzerland. This article is an open access article distributed under the terms and conditions of the Creative Commons Attribution (CC BY) license (<http://creativecommons.org/licenses/by/4.0/>).